



Quantum image edge detection using improved Sobel mask based on NEQR

R. Chetia^{1,2} · S. M. B. Boruah² · P. P. Sahu²

Received: 29 March 2020 / Accepted: 16 November 2020 / Published online: 8 January 2021
© Springer Science+Business Media, LLC, part of Springer Nature 2021

Abstract

Recently, image edge detection using quantum image processing has focused due to having less circuit complexity and storage capacity. Edge extraction using the Sobel operator has the restriction in vertical and horizontal directions, which provides less edge information. In this paper, we introduce a quantum improved Sobel edge detection algorithm with non-maximum suppression and double threshold techniques for novel enhanced quantum representation method. We have analyzed the quantum circuit of realizing the edge detection algorithm, the number of edge pixels, simulation results, and circuit complexity. Thereafter, we have compared with the classical and some existing quantum edge detection algorithms. Our proposed algorithm can achieve a significant improvement in the case of edge information and circuit complexity.

Keywords Quantum image processing · Improved Sobel operator · NEQR · Circuit complexity · Edge detection · Non-maximum suppression

1 Introduction

In digital image processing, the edge is an important feature to determine the property and structure of objects in an image. Edges usually recognized at the boundary between two dissimilar regions in an image and significant local changes of intensity in the image. The edge detection technique is often used in image processing to recover the useful information from images and minimize the quantity of data for further processing. The edge detection technique has many practical applications such as fingerprint recognition, face recognition, medical imaging, automatic traffic controlling systems, location of objects in satellite images, and surgery diagnosis.

✉ R. Chetia
rajibofcit@gmail.com

¹ Department of ECE, Central Institute of Technology (CIT) Kokrajhar, Kokrajhar, BTAD, Assam 783370, India

² Department of ECE, Tezpur University, Napaam, Tezpur, Assam 784028, India

The classical operator-based edge detection techniques such as Sobel, Prewitt, LoG, and Canny were globally established algorithms for the detection of edges, but they are sensitive to noise images. All the classical edge detection techniques based on operator are not completely suitable in the actual world. Recently, quantum image processing (QIP) has been focused on quantum image edge extraction algorithms utilizing unique properties of quantum mechanics such as entanglement, parallelism, superposition [1], and quantum computation technology. Only n qubits are required for storing information in quantum representation instead of $2^n \times n$ bits needed for storing the same information in a classical representation [2]. QIP utilizes the advantage of these properties. As a result, QIP algorithms are faster than the classical algorithms and significantly increase in quantum storage capacity.

Quantum image processing (QIP) generally has three steps: representation of the quantum image, processing quantum image using quantum computing, and finally measurement of image information from processed quantum images. In quantum-inspired and classically inspired quantum approaches [3–5], the classical image is properly represented in terms of qubit representation. Quantum image representation methods such as qubit lattice [6, 7], flexible representation of quantum image (FRQI) [8], novel enhanced quantum representation (NEQR) [9], quantum log-polar images [10], normal arbitrary quantum superposition state [11], generalized quantum image representation (GQIR) [12, 13] have been reported in different quantum image edge detection algorithms. Many works related to QIP that have been reported mainly include: quantum image scrambling [14–17], quantum image geometric transformation [18, 19], quantum image scaling [20], quantum image encryption and decryption [21], quantum image steganography [22], watermarking of quantum image [23, 24], quantum audio [25], quantum movie [26], quantum image segmentation [27], and quantum image matching [28]. The quantum image edge extraction has already been reported on the basis of different classical operators using FRQI [29], GQIR [30], and NEQR [31–35] representation method. In the FRQI method, it captures the color information as well as position information of every pixel and represents them into quantum state. In this method, the probability amplitude of a single qubit is used to store the image information of the pixel. Therefore, FRQI model cannot retrieve the accurate image. The complexity for preparing the quantum image of FRQI model is $O(2^{4n})$. All these drawbacks are overcome in the NEQR model. On the other hand, GQIR generates row and column redundancy. Although the GQIR method is similar to NEQR except for the independence of the size of the scaled image, the NEQR method is simple, deterministic, and low computational complexity. An enhanced quantum image edge extraction algorithm with Laplacian filtering is already reported to resolve the real-time problem of edge extraction [32]. However, the Laplacian operator is sensitive to noise due to the second derivative operation, and hence, the edge information is to be lost. Recently, the improved quantum Sobel operator based on GQIR representation [30] has been reported to resolve the problem of accurate edge information. But high computational complexity is obtained in comparison with other quantum edge extraction methods [31, 32]. We have already used the Sobel operator having four-directional extraction in QIP [33], but very less improvement of extracted images is noticed in comparison with the classical Sobel operator [36, 37]. Moreover, manually setting a threshold for detecting

edge information with existing techniques provides the inclusion of false edges and missing of actual weak edges [30–33].

In this paper, the quantum edge extraction using Sobel operator with 45° and 135° direction masks is used for the estimation of every pixel's gradient. The non-maximum suppression technique with double threshold values is used to accomplish the sharp and more edge information. Our algorithm based on NEQR exhibits reduced circuit complexity in comparison with the recently reported quantum image edge extraction algorithm [30]. Our proposed algorithm can be achieved by sharper and more edge information than the existing algorithms [31, 33, 36, 37].

We have organized this paper as follows: Section 2 introduces the NEQR method with example, four directions of the classical Sobel edge detection algorithm [36, 37] and non-maximum suppression. Section 3 introduces our quantum image edge detection algorithm, steps of the algorithm and their quantum states equations, and quantum circuit design for the edge detection algorithm. Section 4 analyzes the computational complexity, and simulation experiments of some standard images on classical computer are reported. In Sect. 5, we provide concluding remarks. Appendix 1 describes the algorithm of classical Sobel edge extraction, Appendix 2 describes the quantum image cyclic shift transformations, Appendix 3 gives the quantum arithmetic operations, and Appendix 4 gives a comparison of peak-signal-to-noise ratio (PSNR) and mean square error (MSE) between Sobel-based edge extraction algorithms.

2 Related work

Many works related to the Sobel operator based on the NEQR method [31–35] have been reported for the edge detection algorithms. As our works are also related to NEQR, four-direction Sobel mask, and non-maximum suppression technique, we briefly discuss in this section.

2.1 NEQR

In the NEQR model [9], two entangled qubit sequences are employed for storing the grayscale value and all the pixel coordinates of an image in superposition states [1]. Image operation can be performed conveniently, especially for both partial and statistical color operations. The NEQR method is a deterministic image retrieval method. Therefore, the classical image can be accurately retrieved from the quantum image.

The workflow of preparing NEQR model is shown in Fig. 1a, and a simple NEQR image of size 2×2 is shown in Fig. 1b.

The quantum states of Fig. 1b can be represented as

$$\begin{aligned} |I\rangle &= \frac{1}{2}(|0\rangle \otimes |00\rangle + |120\rangle \otimes |01\rangle + |220\rangle \otimes |10\rangle + |255\rangle \otimes |11\rangle) \\ &= \frac{1}{2}(|00000000\rangle \otimes |00\rangle + |01111000\rangle \otimes |01\rangle + |11011100\rangle \otimes |10\rangle \\ &\quad + |11111111\rangle \otimes |11\rangle) \end{aligned}$$

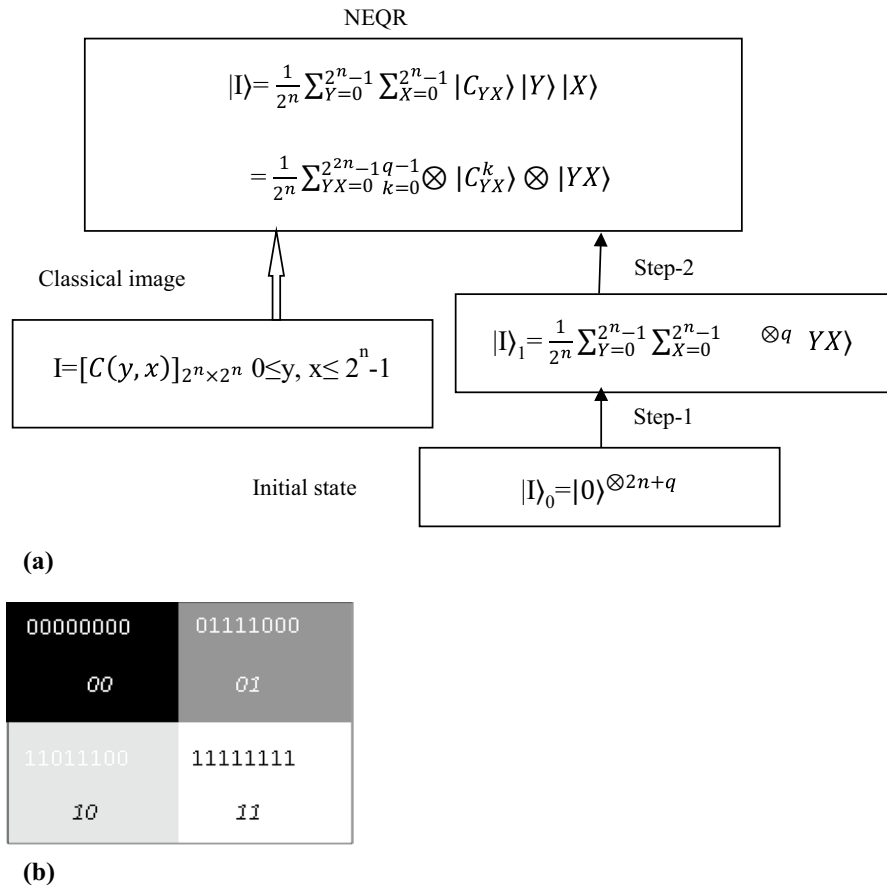


Fig. 1 **a** Workflow of preparing NEQR model. **b** A simple example of 2×2 image and its NEQR state

NEQR expression for a $2^n \times 2^n$ image is written as

$$\begin{aligned}
 |I\rangle &= \frac{1}{2^n} \sum_{Y=0}^{2^n-1} \sum_{X=0}^{2^n-1} |C_{YX}\rangle |Y\rangle |X\rangle \\
 &= \frac{1}{2^n} \sum_{YX=0}^{2^{2n}-1} \otimes^{q-1} |C_{YX}^k\rangle \otimes |YX\rangle
 \end{aligned} \tag{1}$$

where binary sequence encodes the grayscale value C_{YX} of the corresponding pixel coordinate (Y, X) as $C_{YX} = C_{YX}^{q-1} C_{YX}^{q-2} \dots C_{YX}^1 C_{YX}^0$; $C_{YX}^k \in \{0, 1\}$; $C_{YX} \in [0, 2^q - 1]$

We have used the NEQR [1] method because the representation of the quantum image is similar to the classical image representation. Due to superposition states' representation, the number of qubits' requirement will be less than the bits' requirement of classical image representation. NEQR utilizes the quantum

states of superposition to store all the pixels of the image; therefore, all the pixels' data can be processed simultaneously.

2.2 Classical Sobel edge detection

Sobel operator has two sets of 3×3 masks (Appendix 1) and only used to detect the edges of horizontal and vertical directions. Four directions of 3×3 Sobel templates are used for more accurately detecting the image edge points and minimizing the effect of noise on direction. The gradient (G) of every pixel is expressed in horizontal (H), vertical (V), 45° and 135° directions. So, the total gradient of each pixel is estimated as [30, 34]

$$G \cong \max\{|G^V|, |G^H|, |G^{D1}|, |G^{D2}|\} \quad (2)$$

where G^H = gradient in the horizontal direction, G^V = gradient in the vertical direction, G^{D1} = gradient in 45° direction and G^{D2} = gradient in 135° direction.

The pixel will be the part of the edge if $G \geq T$ (Threshold). Figure 2a shows neighborhood templates representing a 3×3 pixel window. Figure 2b, c indicates vertical Sobel mask and horizontal Sobel mask, respectively, whereas 45° direction and 135° direction Sobel masks are represented in Fig. 3a, b, respectively.

2.3 Non-maximum suppression method

Non-maximum suppression is a technique of suppressing all the non-local maximum pixels from the gradient information of the current image. If the gradient value of the current pixel is smaller than the adjacent gradient values, the current pixel point is adjudicated as a non-maximum value and set to zero. If the pixel is greater than and equal to the adjacent gradient value, the current pixel point is adjudicated as a maximum value, and it is to be retained. This technique is applied to find the "largest edge" in edge detection schemes. In this paper, we have calculated the gradient amplitudes in all four directions (i.e., 0° , 45° , 90° and 135°) using the Sobel operator. The non-maximum suppression technique of gradient amplitude image $G(X, Y)$ at (X, Y) coordinate is applied as follows

$S(i-1,j-1)$	$S(i-1,j)$	$S(i-1,j+1)$	-1	-2	-1	-1	0	1
$S(i,j-1)$	$S(i,j)$	$S(i,j+1)$	0	0	0	-2	0	2
$S(i+1,j-1)$	$S(i+1,j)$	$S(i+1,j+1)$	1	2	1	-1	0	1
(a)			(b)			(c)		

Fig. 2 a 3×3 neighborhood templates, b, c two Sobel masks

-2	-1	0
-1	0	1
0	1	2

(a)

0	1	2
-1	0	1
-2	-1	0

(b)

Fig. 3 **a** 45 degree direction, **b** 135 degree direction

$$\begin{aligned}
 M(X, Y) &= G(X, Y) \geq G(X-1, Y) \& G(X, Y) \geq G(X+1, Y) \& G(X, Y) \\
 &\geq G(X-1, Y+1) \& G(X, Y) \geq G(X+1, Y-1) \& G(X, Y) \geq G(X, Y-1) \& G(X, Y) \\
 &\geq G(X, Y+1) \& G(X, Y) \geq G(X-1, Y-1) \& G(X, Y) \geq G(X+1, Y+1)
 \end{aligned}
 \tag{3}$$

where $M(X, Y)=1$ in case of maximum current pixel point and $M(X, Y)=0$ in case non-maximum current pixel point.

3 Quantum image edge detection algorithm

Figure 4 represents a workflow of the algorithm based on four-direction Sobel mask, comprising mainly six steps—quantum image representation, quantum image shift, estimation of quantum pixel gradient, non-maximum suppression, comparison with double thresholds, and edge point estimation

In step 1 of the flowchart, the original image is represented into NEQR quantum image $|I\rangle$. In Step 2, *cyclic shift transformation* (Appendix 2 for details) is used to get the shifted NEQR quantum image set. In step 3, the gradient of each pixel is computed by using the improved Sobel mask and stores those as a gradient $|G\rangle$. In step 4, non-maximum suppression technique is applied to find the maximum gradient amplitude value $|G^S\rangle$ of the local pixel point through the adjacent gradient values. In step 5, all the gradients are compared with the double threshold values (i.e., high $|T_H\rangle$ and low $|T_L\rangle$) through comparators and quantum division (QD) circuit [34, 38]. If each of $|G^S\rangle$ value is greater than and equal to $|T_H\rangle$ or $|T_L\rangle$, then the edge points are found. Finally, in step 6, edge points are estimated ($|E_D\rangle = ||G_L - G_H||$) using quantum absolute value module (QAV) (Appendix 3.1) for image retrieval.

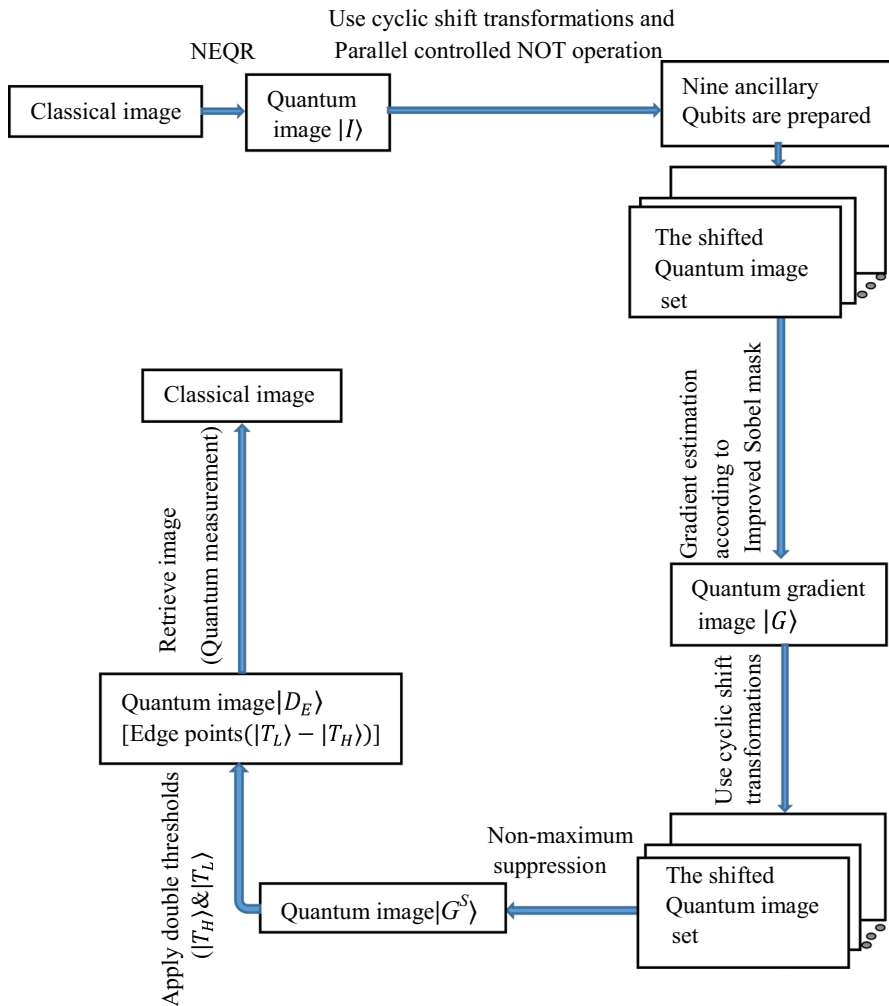


Fig. 4 Workflow of our proposed algorithm

Step 1 The quantum image $|I\rangle$ is prepared using the NEQR method. To store $2^n \times 2^n$ size of an image, $(2n + q)$ qubits are required. The eight extra qubits are needed to record the 3×3 neighborhood pixel window. Parallel-controlled NOT (CNOT) operation is used to copy the nine neighborhood pixels. These quantum image sets can be obtained by tensor product of extra qubits and quantum image $|I\rangle$, i.e.,

$$\begin{aligned}
|0\rangle^{\otimes 8q} \otimes |I_{YX}\rangle &= \frac{1}{2^n} \sum_{Y=0}^{2^n-1} \sum_{X=0}^{2^n-1} |0\rangle^{\otimes 8q} |C_{YX}\rangle |Y\rangle |X\rangle \\
&= \frac{1}{2^n} \sum_{Y=0}^{2^n-1} \sum_{X=0}^{2^n-1} |0\rangle^{\otimes q} \dots |0\rangle^{\otimes q} |C_{YX}\rangle |Y\rangle |X\rangle
\end{aligned} \quad (4)$$

Step 2 We can obtain neighborhood pixels of the whole image $|I_{YX}\rangle$ after the steps of 2–10 in the algorithm (Table 2) and store them into the prepared extra qubits. In this step, parallel controlled NOT operations and certain cyclic shift transformations (Appendix 2) are the main operations used on the original quantum image $|I_{YX}\rangle$ simultaneously to get the eight shifted quantum image sets of any 3×3 neighborhood pixels window of $|I_{YX}\rangle$. In the latter, any eight 3×3 neighborhood pixels of $|I_{YX}\rangle$ are determined and stored in the quantum states. The shifted quantum image sets can be encoded as follows

$$\begin{aligned}
&\frac{1}{2^n} \sum_{Y=0}^{2^n-1} \sum_{X=0}^{2^n-1} |C_{Y-1,X}\rangle \otimes |C_{Y-1,X+1}\rangle \otimes |C_{Y,X+1}\rangle \otimes |C_{Y+1,X+1}\rangle \otimes |C_{Y+1,X}\rangle \\
&\otimes |C_{Y+1,X-1}\rangle \otimes |C_{Y,X-1}\rangle \otimes |C_{Y-1,X-1}\rangle \otimes |C_{Y,X}\rangle |Y\rangle |X\rangle
\end{aligned} \quad (5)$$

Step 3 The gradient calculation of every pixel of the image $|I\rangle$ in vertical, horizontal, 45° and 135° directions is defined as follows

$$\begin{aligned}
||G_{YX}^V\rangle| &= |(|C_{Y+1,X-1}\rangle + 2|C_{Y+1,X}\rangle + |C_{Y+1,X+1}\rangle) - (|C_{Y-1,X-1}\rangle + 2|C_{Y-1,X}\rangle \\
&\quad + |C_{Y-1,X+1}\rangle)| \\
||G_{YX}^H\rangle| &= |(|C_{Y-1,X+1}\rangle + 2|C_{Y,X+1}\rangle + |C_{Y+1,X+1}\rangle) - (|C_{Y-1,X-1}\rangle + 2|C_{Y,X-1}\rangle \\
&\quad + |C_{Y+1,X-1}\rangle)| \\
||G_{YX}^{D1}\rangle| &= |(|C_{Y,X+1}\rangle + 2|C_{Y+1,X+1}\rangle + |C_{Y+1,X}\rangle) - (|C_{Y-1,X}\rangle + 2|C_{Y-1,X-1}\rangle \\
&\quad + |C_{Y,X-1}\rangle)| \\
||G_{YX}^{D2}\rangle| &= |(|C_{Y-1,X}\rangle + 2|C_{Y-1,X+1}\rangle + |C_{Y,X+1}\rangle) - (|C_{Y,X-1}\rangle + 2|C_{Y+1,X-1}\rangle \\
&\quad + |C_{Y+1,X}\rangle)|
\end{aligned}$$

So, the overall gradient of each individual pixel is estimated as [30, 34]

$$|G\rangle \cong \max\{|G_{YX}^V\rangle|, |G_{YX}^H\rangle|, |G_{YX}^{D1}\rangle|, |G_{YX}^{D2}\rangle|\} \quad (6)$$

According to Eq. (6), quantum arithmetic operations (Appendix 3) are employed to determine each pixel gradient. The absolute values of sub-gradients $|G_{YX}^H\rangle$, $|G_{YX}^V\rangle$, $|G_{YX}^{D1}\rangle$, and $|G_{YX}^{D2}\rangle$ are estimated in all four directions by using three quantum comparators [43], and the desired output gradient values $|G\rangle$ can be represented as

$$\frac{1}{2^n} \sum_{Y=0}^{2^n-1} \sum_{X=0}^{2^n-1} |N\rangle |G_{Y,X}^i\rangle |Y\rangle |X\rangle \quad (7)$$

where $i = V, H, D_1, D_2$; $|N\rangle, |G_{Y,X}^i\rangle = 1$ for gradient values and $|N\rangle, |G_{Y,X}^i\rangle = 0$ for non-gradient values.

The encoded quantum state $|G\rangle$ can be written as follows

$$|0\rangle \otimes |G\rangle = \frac{1}{2^n} \sum_{Y=0}^{2^n-1} \sum_{X=0}^{2^n-1} |0\rangle |N\rangle G_{Y,X}^i |Y\rangle |X\rangle \quad (8)$$

Circuit implementation for Eqs. (4)–(8) is shown in Figs. 5, 6 and 7. All the garbage qubits are ignored and not shown in the circuits.

Step 4 Eight quantum comparators are employed to find the local maximum gradient pixel $|G^S\rangle$ of the gradient image $|G\rangle$ obtained from improved Sobel operation. Similar to the step 2, we first prepare nine copies of quantum image $|G\rangle$ and then use cyclic shift transformation to acquire the information of every pixel of the 3×3 neighborhood window. All the 3×3 neighborhood pixels are stored in extra ancillary qubits. According to Eq. (3), the quantum arithmetic operations are performed for the non-maximum suppression in the image $|G\rangle$. The quantum circuit realization of non-maximum suppression is shown in Fig. 8, and the output quantum states $|G^S\rangle$ can be represented as

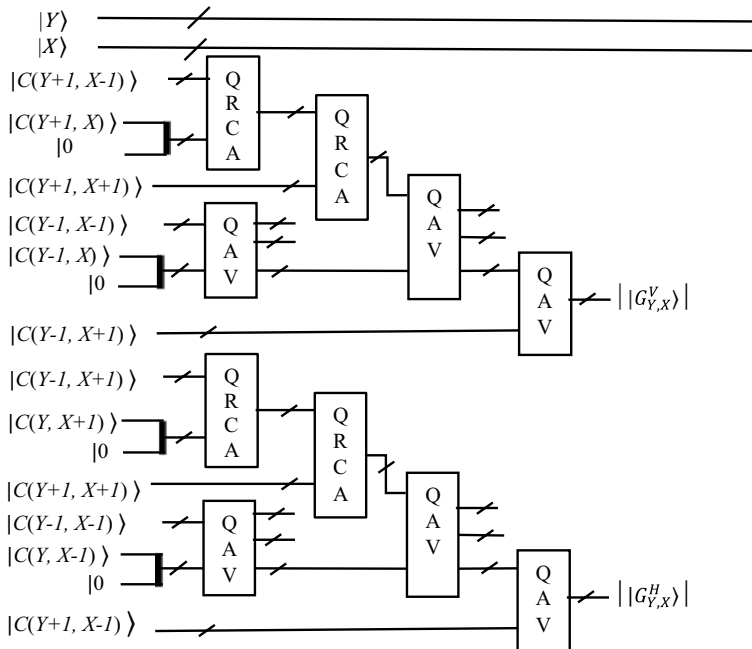


Fig. 5 Quantum circuit realization for gradient estimation of a quantum image into the vertical and horizontal directions

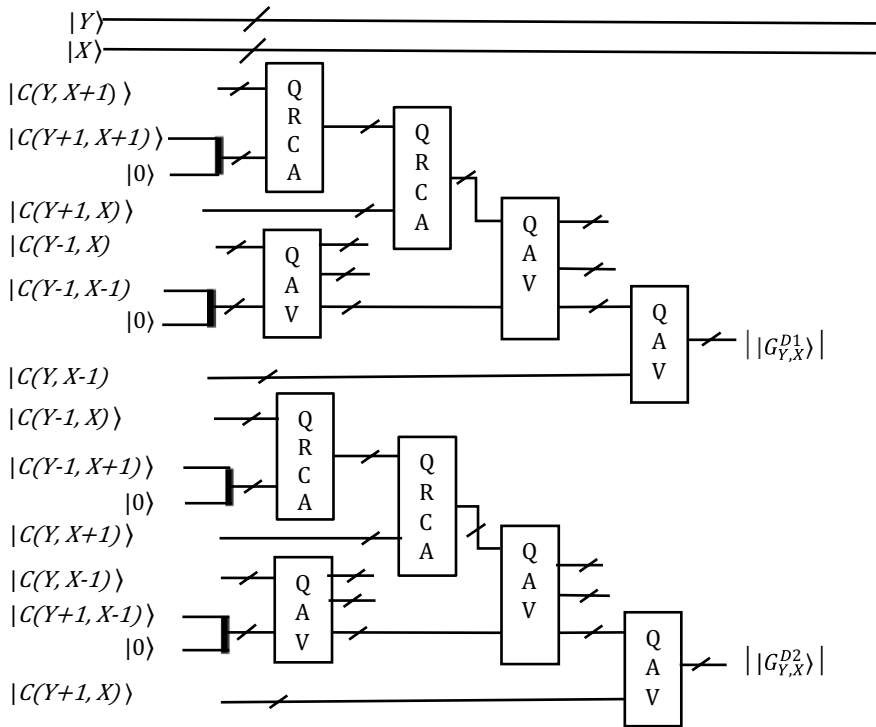


Fig. 6 Quantum circuit realization for gradient estimation of a quantum image into the diagonal directions

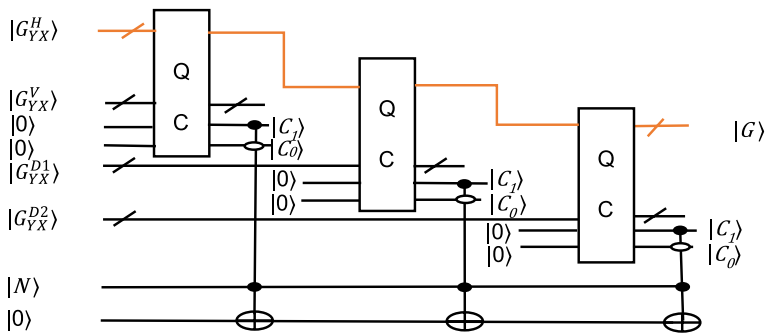


Fig. 7 Quantum circuit realization of gradient estimation of image

$$|G^S\rangle = \frac{1}{2^n} \sum_{Y=0}^{2^n-1} \sum_{X=0}^{2^n-1} |M\rangle |G_{YX}\rangle |Y\rangle |X\rangle \quad (9)$$

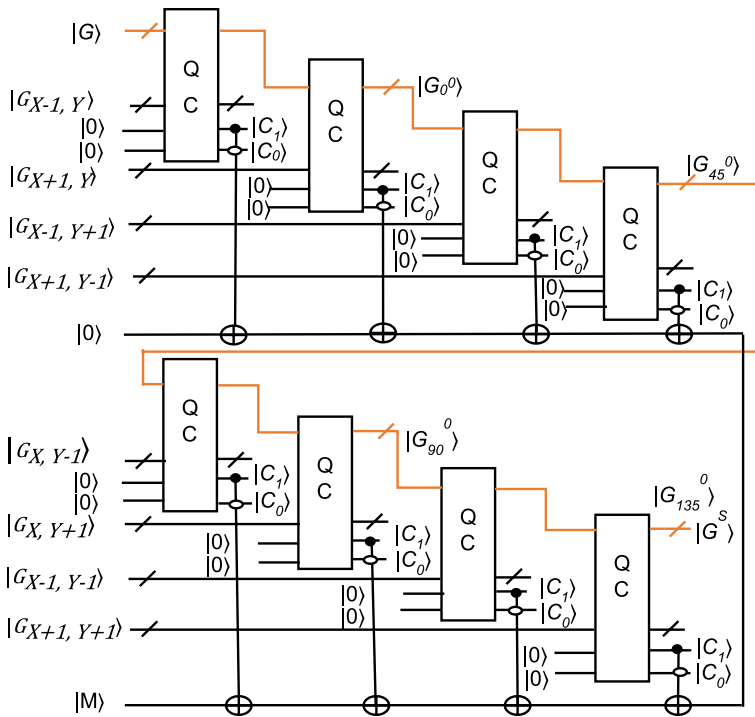


Fig. 8 Quantum circuit realization of non-maximum suppression

where $|M\rangle = 1$ for the maximum current pixel point and $|M\rangle = 0$ for non-maximum current pixel point.

Step 5 Similar to the step 4, 3×3 neighborhood pixels are stored in extra auxiliary qubits and compared the gradient values in all four directions (i.e., 0° , 45° , 90° and 135°) using double thresholds ($|T_H\rangle$ & $|T_L\rangle$). The relation between high threshold and low threshold is $|T_L\rangle = \frac{1}{|\alpha|} |T_H\rangle$, where $|\alpha| = 3$. The low threshold value is estimated by using the quantum division circuit (QD) [34, 38]. If the gradient value is greater than and equal to $|T_H\rangle$ or $|T_L\rangle$, strong or weak edge points are obtained. The quantum states of double thresholds can be written as follows

$$|T_H\rangle = \frac{1}{2^n} \sum_{Y=0}^{2^n-1} \sum_{X=0}^{2^n-1} |M\rangle |G_{Y-1,X}^S\rangle |G_{Y-1,X+1}^S\rangle |G_{Y,X+1}^S\rangle |G_{Y+1,X+1}^S\rangle |G_{Y+1,X}^S\rangle |G_{Y+1,X-1}^S\rangle |G_{Y,X-1}^S\rangle |G_{Y-1,X-1}^S\rangle |Y\rangle |X\rangle \quad (10)$$

$$|T_L\rangle = \frac{1}{3 \times 2^n} \sum_{Y=0}^{2^n-1} \sum_{X=0}^{2^n-1} |M\rangle |G_{Y-1,X}^S\rangle |G_{Y-1,X+1}^S\rangle |G_{Y,X+1}^S\rangle |G_{Y+1,X+1}^S\rangle |G_{Y+1,X}^S\rangle |G_{Y+1,X-1}^S\rangle |G_{Y,X-1}^S\rangle |G_{Y-1,X-1}^S\rangle |Y\rangle |X\rangle \quad (11)$$

The threshold value is estimated from one-third grayscale value of 3×3 neighborhood pixel.

Step 6 In order to classify the more accurate edge pixels, high threshold $|T_H\rangle$ pixel value is subtracted from the low threshold $|T_L\rangle$ pixel value using the quantum absolute value module (Appendix 3.1). Similarly, extra ancillary qubits are employed to store the 3×3 neighborhood pixels. The final state of the extracted edge pixels can be represented as follows

$$|D_E\rangle = \frac{1}{2^n} \sum_{Y=0}^{2^n-1} \sum_{X=0}^{2^n-1} |M\rangle |D_{YX}\rangle |Y\rangle |X\rangle; D_{Y,X} \in \{0, 1\} \quad (12)$$

where $M, D_{Y,X}=0$ in case of non-edge point and $M, D_{Y,X}=1$ in case of edge point. The quantum circuit realization of edge points is shown in Fig. 9.

3.1 Quantum circuit design for edge detection algorithm

To realize the quantum circuit of the algorithm, we have employed the quantum image cyclic shift transformations (Appendix 2), parallel-controlled NOT operations (Appendix 3.2), quantum operation for multiplication with 2^n (Appendix 3.3), quantum ripple-carry adder (QRCA) (Appendix 3.4), quantum absolute value (QAV) module (Appendix 3.1), quantum division (QD) circuit [34, 38], and quantum comparator (QC) (Appendix 3.5).

4 Results and discussion

4.1 Computational complexity

We have considered a $2^n \times 2^n$ size of digital image for evaluation of circuit complexity of our algorithm. Computational complexity is estimated here in four stages:

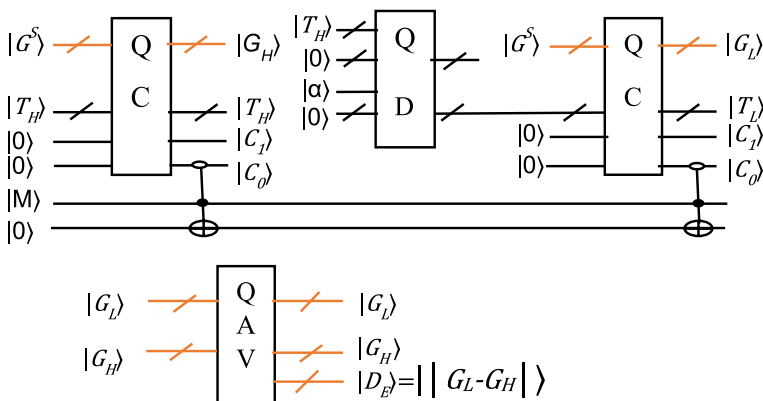


Fig. 9 Quantum circuit realization of edge points

quantum image construction, four-direction-based Sobel operators to calculate the gradient value, non-maximum suppression, and extraction of edge points.

4.1.1 Quantum image construction

The computational complexity for the representation of the quantum image ($|I\rangle$) using NEQR is derived $O(qn2^{2n})$ [9].

4.1.2 Four-direction-based Sobel operator to calculate the gradient value

As mentioned, there are two processes at this stage: shift transformation [19, 39] with parallel CNOT operation and calculation of the gradient of every pixel values in Sobel-filtered image. The time complexity of each shift transformation has derived as $O(n^2)$ [39], and the time complexity for each parallel CNOT gate operation is $O(q)$. We have used eight numbers of quantum ripple-carry adder (QRCA) modules to estimate the sum of two n -bit numbers and twelve numbers of quantum absolute value (QAV) modules to calculate the absolute gradient values. The circuit complexity of each q -qubit QRCA module is derived as $O(q)$ [40], and the QAV module is estimated [41, 42] as $O(q^2)$. However, the circuit complexity of a single QD is $3q^3 + 6q^2 + q$ [34, 38]. So the circuit complexity for this stage can be written as $O(n^2 + q^3)$.

4.1.3 Non-maximum suppression

This process is similar to the above process. The parallel-controlled NOT operation is used to copy the nine extra image copies and 3×3 neighborhood pixels. In this process, eight QC modules are used to find the maximum gradient pixel. The circuit complexity of this stage is $O(n^2 + q^2)$.

4.1.4 Extraction of edge points

In this process, two QC modules, one QD module, and one QAV module are employed to detect the edge points and non-edge points. Two q -qubit integers are used [41] in two QC modules. So the complexity of this stage is $O(n^2 + q^3)$.

Usually, the circuit complexity of quantum image preparation and measurement processes are not considered in the quantum image algorithm. Therefore, the overall circuit complexity of our scheme based on NEQR for a $2^n \times 2^n$ size of a digital image is written as $\sim O(n^2 + q^3)$, which provides an exponential speedup. In Table 1, computational complexity of the algorithm is compared with other edge detection schemes (Fig. 10).

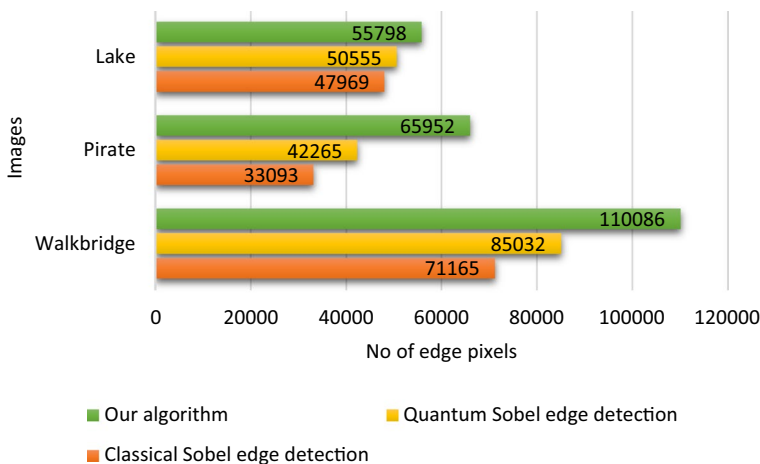
4.2 Simulation analysis

The simulations of our algorithm are made on grayscale images represented in terms of NEQR by using a classical computer. The simulations are based on linear

Table 1 The complexity comparison of Sobel edge extraction schemes

Algorithm	QIR model	Complexity
Sobel [36, 37]	–	$O(2^{2n})$
Zhang [29]	FRQI	$O(n^2)$
Fan [31]	NEQR	$O(n^2 + 2^{q+4})$
Zhou [30]	GQIR	$O(n^2 + 2^{q+5} + q^2)$
Our scheme	NEQR	$O(n^2 + q^3)$

algebra, and quantum states (qubits) expressed as a complex vector, and the unitary matrices act as unitary transforms. The simulations of our algorithm for several grayscale images have performed using MATLAB 9.4.0 (R2018a) and run on a classical computer with Intel® Core™i58300H CPU @ 2.30 GHz, 8.00 GB RAM (OS 64-bit). The NEQR method is used in this paper to represent the images. Therefore, the size of the image should be $2^n \times 2^n$. We have taken three common standard test images [49]—Pirate, Walk Bridge and Lake—as mentioned in Fig. 11a with a size of 512×512 . We have also computed edge detection using the existing quantum Sobel operator [31] and classical Sobel operator [36, 37] for the comparison with our technique. The non-maximum suppression technique and double threshold values are used in our algorithm to estimate the edge points. As a result, we have obtained more edge information as well as sharp edge contours due to the non-maximum suppression operation. Our algorithm provides extraction of more edge information with sharp edges than that of other existing techniques [31, 36, 37], as seen from Fig. 11b–d. We have estimated the number of edge pixels (NoEP) of extract

**Fig. 10** Edge information graph for classical Sobel, quantum Sobel and our edge detection algorithm

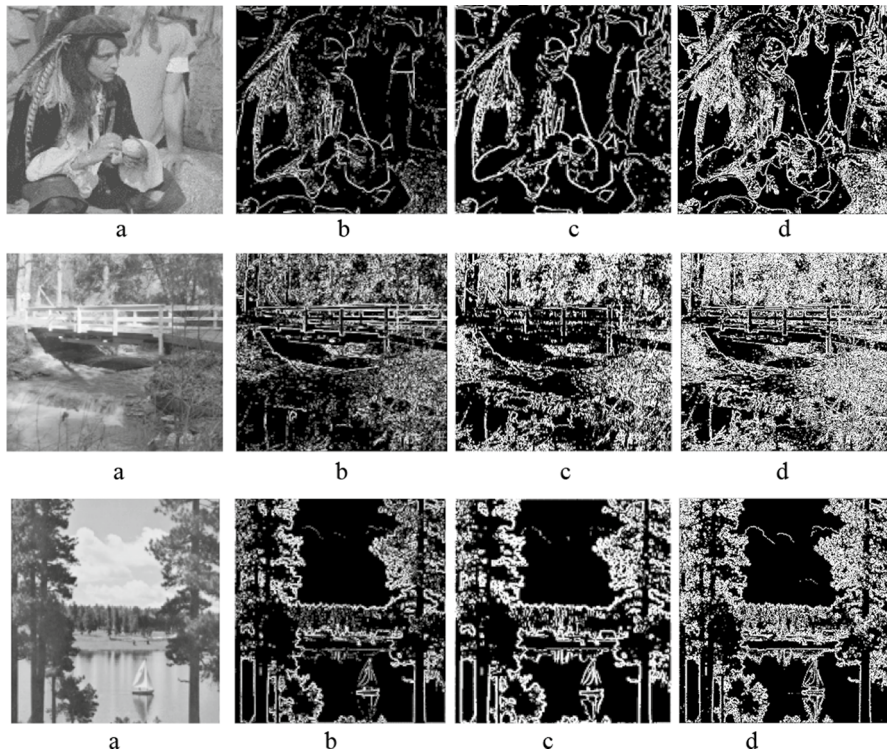


Fig. 11 **a** Three common and standard test images—Pirate—Walk bridge—Lake [49]. **b** Classical Sobel edge extracted images of Pirate, Walk bridge and Lake [36, 37]. **c** Quantum Sobel edge extracted images of Pirate, Walk bridge and Lake [31]. **d** Edge extracted images of our algorithm

images by using the classical Sobel operator, existing quantum Sobel operator, and our algorithm. The number of edges pixels obtained using our technique in all four images is more than those obtained using existing techniques due to the use of four directional extraction with double threshold, as shown in Fig. 10. It is seen from the figures that the extracted images of our algorithm contain more edge information than that of the other two existing techniques [31, 36, 37].

We have also estimated the PSNR and MSE values of the extracted images, as described in Appendix 4.

5 Conclusion

We have presented an improved quantum Sobel edge detection algorithm using non-maximum suppression technique and double threshold values to obtain more edge information with a sharper edge. The extracted edges of the image are more

specific and distinct than those extracted by existing algorithms. The quantum circuit realization of our algorithm is reported that the circuit complexity can achieve exponential speedup over all classical edge detection algorithms. Moreover, discontinuity, roughness, and other defects can be removed by using our method. The algorithm is more effective in the edge extraction of images due to insensitive to noise. Our future works will be to develop the algorithm for the edge extraction of biomedical images.

Appendix 1: Classical Sobel edge extraction algorithm

Sobel operator is an individually separate and distinct differential operator. Sobel operator has two sets of 3×3 masks and mainly used for edge detection of an image (Fig. 12).

If G^H and G^V represent the image gradient values of the original image into the horizontal and vertical directions, then the calculation of G^H & G^V is defined as

$$\begin{aligned}
 G^H &= -1 \times S(Y-1, X-1) + 0 \times S(Y-1, X) + 1 \times S(Y-1, X+1) + (-2) \\
 &\quad \times S(Y, X-1) + 0 \times S(Y, X) + 2 \times S(Y, X+1) + (-1) \times S(Y+1, X-1) + 0 \times S(Y+1, X) + 1 \\
 &\quad \times S(Y+1, X+1) \\
 &= S(Y-1, X+1) + 2S(Y, X+1) + S(Y+1, X+1) - S(Y-1, X-1) \\
 &\quad - 2S(Y, X-1) - S(Y+1, X-1)
 \end{aligned} \tag{13}$$

$S(i-1, j-1)$	$S(i-1, j)$	$S(i-1, j+1)$	-1	-2	-1	-1	0	1
$S(i, j-1)$	$S(i, j)$	$S(i, j+1)$	0	0	0	-2	0	2
$S(i+1, j-1)$	$S(i+1, j)$	$S(i+1, j+1)$	1	2	1	-1	0	1

(a)
(b)
(c)

Fig. 12 **a** 3×3 pixel neighborhood templates, **b** and **c** two operators of Sobel algorithm

$$\begin{aligned}
G^V &= -1 \times S(Y-1, X-1) + (-2) \times S(Y-1, X) + (-1) \times S(Y-1, X+1) + 0 \\
&\quad \times S(Y, X-1) + 0 \times S(Y, X) + 0 \times S(Y, X+1) + 1 \times S(Y+1, X-1) + 2 \\
&\quad \times S(Y+1, X) + 1 \times S(Y+1, X+1) \\
&= S(Y+1, X-1) + 2S(Y+1, X) + S(Y+1, X+1) - S(Y-1, X-1) \\
&\quad - 2S(Y-1, X) - S(Y-1, X+1)
\end{aligned} \tag{14}$$

The total gradient for each pixel is as follows

$$G \cong |G^V| + |G^H| \tag{15}$$

The pixel will be the part of edge if $G \geq T_H$ (Threshold).

Appendix 2: Quantum image cyclic shift transformations

The cyclic shift (X shift and Y shift) transformation is used to shift the position of whole image so that every pixel of the image will get the information of its neighborhood simultaneously [18, 19, 39]. As an example, if we shift one unit upward, the pixel of the image will be transformed $S(x, y)$ into $S(x, y+1)$. The cyclic shift transformation (CT) of quantum image $|I\rangle$ can be expressed as

$$CT(X\pm)|I\rangle = \frac{1}{2^n} \sum_{Y=0}^{2^n-1} \sum_{X=0}^{2^n-1} |CT_{YX'}\rangle |Y\rangle |X \pm 1 \bmod 2^n\rangle \tag{16}$$

$$CT(Y\pm)|I\rangle = \frac{1}{2^n} \sum_{Y=0}^{2^n-1} \sum_{X=0}^{2^n-1} |CT_{Y'X}\rangle |Y \pm 1 \bmod 2^n\rangle |X\rangle \tag{17}$$

where $X' = (X \mp 1) \bmod 2^n$, $Y' = (Y \mp 1) \bmod 2^n$, $CT_{(X+)} \ \& \ CT_{(Y+)} = \begin{bmatrix} 0 & 1 \\ I_2^n - 1 & 0 \end{bmatrix}$ and

$$CT_{(X-)} \ \& \ CT_{(Y-)} = \begin{bmatrix} 0 & I_2^n - 1 \\ 1 & 0 \end{bmatrix}$$

See Fig. 13 and Table 2.

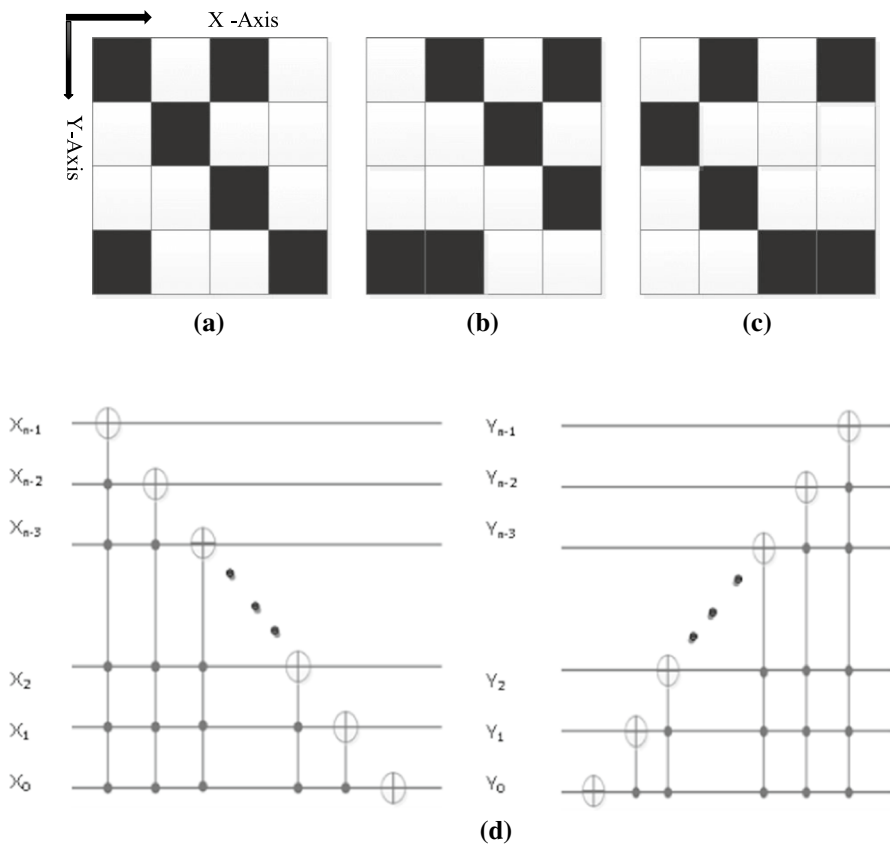


Fig. 13 **a** An example of original image of size 4×4 , **b** the image transformed after $CT(X+)$ operation, **c** the image transformed after $CT(X-)$ operation. **d** Quantum circuit realization of $CT_{(X+)}$ and $CT_{(Y-)}$ for n -qubit sequence

Appendix 3: Quantum arithmetic operations

3.1 Quantum absolute value (QAV) module

Quantum absolute value module is used to estimate the absolute value of two integer number in quantum circuit. Basically, it consists of reversible

Table 2 Computation prepared algorithm for shifting the image

1. Input: the original NEQR image I_{YX} , $|I_{YX}\rangle = \frac{1}{2^n} \sum_{Y=0}^{2^n-1} \sum_{X=0}^{2^n-1} |C_{YX}\rangle |Y\rangle |X\rangle$
2. Shift I_{YX} one unit upward, then $|I_{Y+1X}\rangle = CT(Y-)|I_{YX}\rangle = \frac{1}{2^n} \sum_{Y=0}^{2^n-1} \sum_{X=0}^{2^n-1} |C_{Y+1X}\rangle |Y\rangle |X\rangle$
3. Shift I_{Y+1X} one unit leftward, then $|I_{Y+1X+1}\rangle = CT(X-)|I_{Y+1X}\rangle = \frac{1}{2^n} \sum_{Y=0}^{2^n-1} \sum_{X=0}^{2^n-1} |C_{Y+1X+1}\rangle |Y\rangle |X\rangle$
4. Shift I_{Y+1X+1} one unit downward, then $|I_{YX+1}\rangle = CT(Y+)|I_{Y+1X+1}\rangle = \frac{1}{2^n} \sum_{Y=0}^{2^n-1} \sum_{X=0}^{2^n-1} |C_{YX+1}\rangle |Y\rangle |X\rangle$
5. Shift I_{YX+1} one unit downward, then $|I_{Y-1X+1}\rangle = CT(Y+)|I_{YX+1}\rangle = \frac{1}{2^n} \sum_{Y=0}^{2^n-1} \sum_{X=0}^{2^n-1} |C_{Y-1X+1}\rangle |Y\rangle |X\rangle$
6. Shift I_{Y-1X+1} one unit rightward, then $|I_{Y-1X}\rangle = CT(X+)|I_{Y-1X+1}\rangle = \frac{1}{2^n} \sum_{Y=0}^{2^n-1} \sum_{X=0}^{2^n-1} |C_{Y-1X}\rangle |Y\rangle |X\rangle$
7. Shift I_{Y-1X} one unit rightward, then $|I_{Y-1X-1}\rangle = CT(X+)|I_{Y-1X}\rangle = \frac{1}{2^n} \sum_{Y=0}^{2^n-1} \sum_{X=0}^{2^n-1} |C_{Y-1X-1}\rangle |Y\rangle |X\rangle$
8. Shift I_{Y-1X-1} one unit upward, then $|I_{YX-1}\rangle = CT(Y-)|I_{Y-1X-1}\rangle = \frac{1}{2^n} \sum_{Y=0}^{2^n-1} \sum_{X=0}^{2^n-1} |C_{YX-1}\rangle |Y\rangle |X\rangle$
9. Shift I_{YX-1} one unit upward, then $|I_{Y+1X-1}\rangle = CT(Y-)|I_{YX-1}\rangle = \frac{1}{2^n} \sum_{Y=0}^{2^n-1} \sum_{X=0}^{2^n-1} |C_{Y+1X-1}\rangle |Y\rangle |X\rangle$
10. Shift I_{Y+1X-1} one unit leftward and one unit downward to the original position, then $|I_{YX}\rangle = CT(X-)(CT(Y+)|I_{Y+1X-1}\rangle) = \frac{1}{2^n} \sum_{Y=0}^{2^n-1} \sum_{X=0}^{2^n-1} |C_{YX}\rangle |Y\rangle |X\rangle$

parallel subtractor (RPS) module and complement operation (CO) module [32, 41, 42]. Quantum absolute value module for qubits $|Y\rangle = |Y_{n-1}Y_{n-2} \dots Y_1Y_0\rangle$ and $|X\rangle = |X_{n-1}X_{n-2} \dots X_1X_0\rangle$ is shown in Fig. 14. For more information referred to [4, 5].

3.2 Parallel-controlled NOT (CNOT) operation

CNOT operations are used to copy a quantum states. Parallel CNOT can be used to copy n-qubit quantum states into $|0\rangle^{\otimes n}$ ancillary qubits. The quantum circuit for parallel q-CNOT is shown in Fig. 15.

3.3 Quantum operation for multiplied by 2^n

Quantum operation for the qubit of an integer binary bits (i.e., $|A\rangle = |a_{n-1} a_{n-2} \dots a_1 a_0\rangle$) multiplied by 2^n can be realized as follows.

$$2^n |A\rangle = |a_{n-1} a_{n-2} \dots a_1 a_0 \underbrace{0 \dots 0}_n\rangle, \text{ where } |0\rangle^{\otimes n} \text{ ancillary qubits are added after}$$

the lowest qubit.

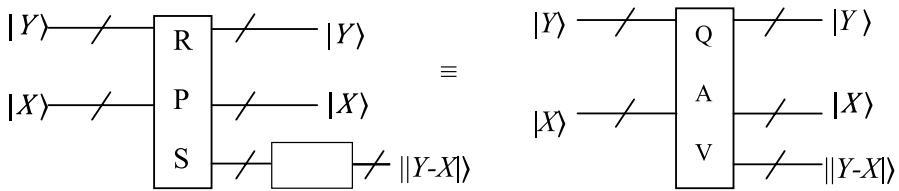


Fig. 14 Quantum circuit of QAV module

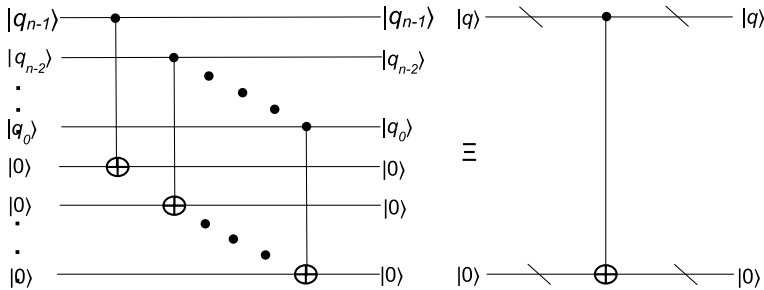


Fig. 15 Quantum circuit for parallel CNOT operations

3.4. Quantum ripple-carry adder (QRCA)

QRCA module [40] can be used to estimate the sum of two n -bit numbers A and B , where $A = a_{n-1}a_{n-2}\dots a_0$, $B = b_{n-1}b_{n-2}\dots b_0$. It consists of two basic modules of MAJ (Majority) gate and UMA (Un Majority and Add) gate [40], which start from low-order bits of the input added with carry to next order bits. In QRCA module, some ancillary and garbage qubits are omitted for simplification. The simplified QRCA module is shown in Fig. 16.

3.5 Quantum comparator (QC)

Quantum comparator [43] is used to compare the relations between two numbers. The output of QC module for two qubit sequence $|A\rangle = |a_{n-1}a_{n-2}\dots a_1a_0\rangle$ and $|B\rangle = |b_{n-1}b_{n-2}\dots b_1b_0\rangle$ can be represented as follows

If $C_1C_0 = 10$, then $|A\rangle > |B\rangle$

If $C_1C_0 = 01$, then $|A\rangle < |B\rangle$

If $C_1C_0 = 00$, then $|A\rangle = |B\rangle$

See Fig. 17.

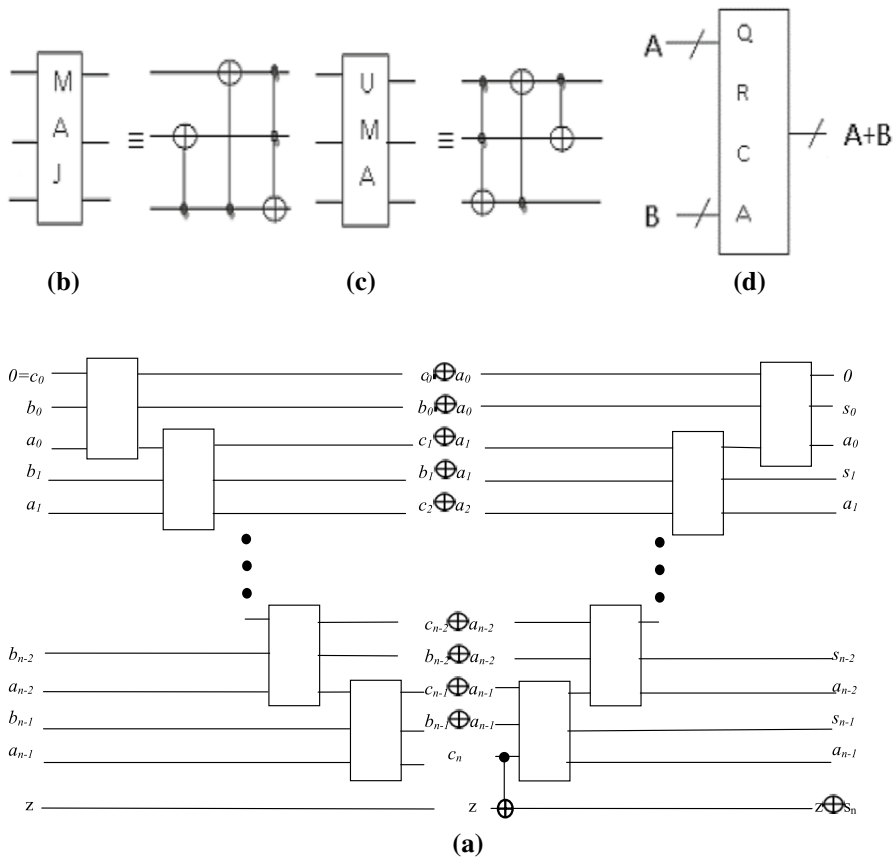


Fig. 16 Quantum circuit realization for **a** n-bit simple ripple-carry adder, **b** MAJ module, **c** UMA module and **d** simplified QRCA module

Appendix 4: Peak-signal-to-noise ratio (PSNR) and mean square error (MSE)

To compare the fidelity of a retrieval image with its original version, the peak-signal-to-noise ratio (PSNR) [44–48] is often used. The PSNR representing an evaluation metric for estimating fidelity of quantum is written as

$$\text{PSNR} = 20 \log_{10} \left(\frac{QMAX_I}{\sqrt{\text{MSE}}} \right) \quad (18)$$

where $QMAX_I$ the maximum pixel value of quantum is mechanically represented image and MSE [44–48] is the mean square error of quantum mechanically represented image. For two $m \times n$ images, MSE can be defined as follows

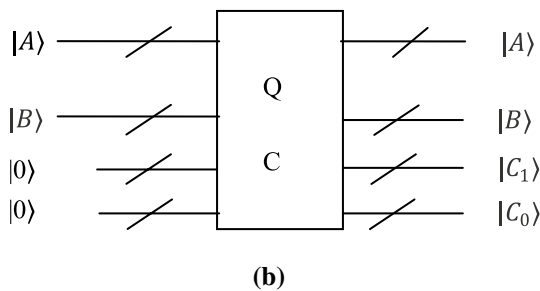
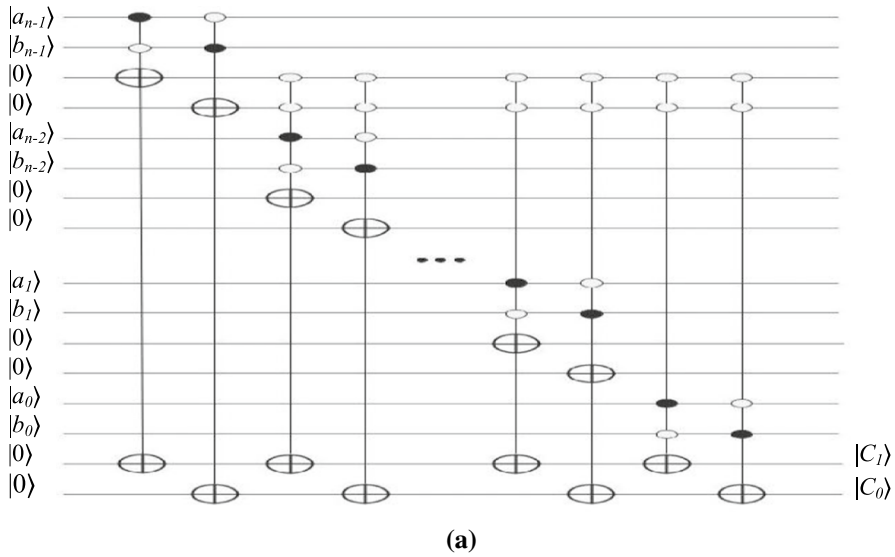


Fig. 17 **a** Quantum circuit for quantum comparator. **b** Quantum module for quantum comparator

$$\text{MSE} = \frac{1}{mn} \sum_{X=0}^{m-1} \sum_{Y=0}^{n-1} [(Q(X, Y) - QR(X, Y))^2] \quad (19)$$

We have considered $m=n$ for simulation. Where $Q(X, Y)$ = Quantum mechanically represented original image with X – Y position coordinates.

Figure 18a shows more PSNR obtained from all four images by using our algorithm than that obtained by the other two existing techniques. More improvement of PSNR value is noticed in walk bridge images than that in other images by using our algorithm, due to having more edge boundary and local changes of intensity in walk bridge image. So our algorithm is comparatively more effective in edge extraction of an image having more boundary and local changes than the

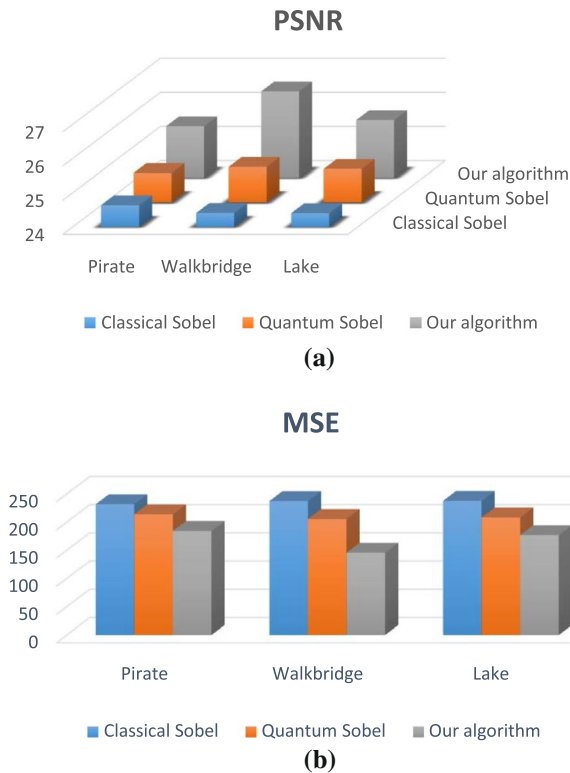


Fig. 18 **a** PSNR graph for classical Sobel, quantum Sobel and our edge detection algorithm. **b** MSE graph for classical Sobel, quantum Sobel and our edge detection algorithm

Table 3 PSNR and MSE values for Sobel-based edge extraction algorithms

Input image	Classical Sobel edge extraction		Quantum Sobel edge extraction		Our algorithm	
	PSNR	MSE	PSNR	MSE	PSNR	MSE
Pirate	24.6384	231.73	24.8629	213.89	25.5098	184.29
Walk bridge	24.4104	237.38	25.0383	205.42	26.529	145.72
Lake	24.4046	237.69	24.9791	208.24	25.6888	176.85

other two algorithms. Figure 18b compares the MSE of extracted images between our algorithm and existing algorithms. The MSE of all extracted images obtained from our algorithm is less than that obtained using existing techniques due to less false edge information (Table 3).

References

1. Yan, F., Iliyasu, A.M., Le, P.Q.: Quantum image processing: a review of advances in its security technologies. *Int. J. Quantum Inf.* **15**(03), 1730001 (2017)
2. Feynman, R.P.: Simulating physics with computers. *Int. J. Theor. Phys.* **21**(6/7), 467–488 (1982)
3. Iliyasu, A.M.: Towards the realization of secure and efficient image and video processing applications on quantum computers. *Entropy* **15**, 2874–2974 (2013)
4. Iliyasu, A.M.: Algorithmic frameworks to support the realization of secure and efficient image-video processing applications on quantum computers. Ph. D. (Dr Eng.) Thesis, Tokyo Institute of Technology, Tokyo, Japan. 25 Sept. 2012 (2012)
5. Iliyasu, A.M., Le, P.Q., Yan, F., Bo, S., Garcia, J.A.S., Dong, F., Hirota, K.: A two-tier scheme for gray-scale quantum image watermarking and recovery. *Int. J. Innov. Comput. Appl.* **5**, 85–101 (2013)
6. Tseng, C.C., Hwang, T.M.: Quantum digital image processing algorithms. In: Proceedings of the 16th IPPR Conference on Computer Vision, Graphics and Image Processing, pp. 827–834 (2003)
7. Venegas-Andraca, S.E., Bose, S.: Storing, processing and retrieving an image using quantum mechanics. In: Proceeding of the SPIE Conference Quantum Information and Computation, vol. 5105, pp. 137–147 (2003)
8. Le, P.Q., Dong, F., Hirota, K.: A flexible representation of quantum images for polynomial preparation, image compression, and processing operations. *Quantum Inf. Process.* **10**(1), 63–84 (2011)
9. Zhang, Y., Lu, K., Gao, Y., et al.: NEQR: a novel enhanced quantum representation of digital images. *Quantum Inf. Process.* **12**(8), 2833–2860 (2013)
10. Zhang, Y., Lu, K., Gao, Y., Xu, K.: A novel quantum representation for log-polar images. *Quantum Inf. Process.* **12**(9), 3103–3126 (2013)
11. Li, H., Zhu, Q., Zhou, R., Song, L., Yang, X.: Multi-dimensional color image storage and retrieval for a normal arbitrary quantum superposition state. *Quantum Inf. Process.* **13**, 991–1011 (2014)
12. Jiang, N., Wang, J., Mu, Y.: Quantum image scaling up based on nearest-neighbor interpolation with integer scaling ratio. *Quantum Inf. Process.* **14**(11), 4001–4026 (2015)
13. Jiang, N., Wu, W.Y., Wang, L., Zhao, N.: Quantum image pseudo color coding based on the density-stratified method. *Quantum Inf. Process.* **14**(5), 1735–1755 (2015)
14. Jiang, N., Wu, W.Y., Wang, L.: The quantum realization of Arnold and Fibonacci image scrambling. *Quantum Inf. Process.* **13**, 1223–1236 (2014)
15. Jiang, N., Wang, L., Wu, W.Y.: Quantum Hilbert image scrambling. *Int. J. Theor. Phys.* **53**, 2463–2484 (2014)
16. Zhou, R.G., Sun, Y.J., Fan, P.: Quantum image Gray-code and bit-plane scrambling. *Quantum Inf. Process.* **14**, 1717–1734 (2015)
17. Arbelaez, P., Maire, M., Fowlkes, C., Malik, J.: Contour detection and hierarchical image segmentation. *IEEE TPAMI* **33**(5), 898–916 (2011)
18. Le, P.Q., Iliyasu, A.M., Dong, F., Hirota, K.: Fast geometric transformations on quantum images. *IAENG Int. J. Appl. Math.* **40**(3), 113–123 (2010)
19. Le, P.Q., Iliyasu, A.M., Dong, F., et al.: Strategies for designing geometric transformations on quantum images. *Theor. Comput. Sci.* **412**, 1406–1418 (2011)
20. Zhou, R.-G., Hu, W., Fan, P., Ian, H.: Quantum realization of the bilinear interpolation method for NEQR. *Sci. Rep.* **7**(1), 2511 (2017)
21. Zhou, R.G., Wu, Q., Zhang, M.Q., et al.: Quantum image encryption and decryption algorithms based on quantum image geometric transformations. *Int. J. Theor. Phys.* **52**(6), 1802–1817 (2013)
22. Jiang, N., Zhao, N., Wang, L.: LSB based quantum image steganography algorithm. *Int. J. Theor. Phys.* **55**(1), 107–123 (2016)
23. Iliyasu, A.M., Le, P.Q., Dong, F., et al.: Watermarking and authentication of quantum image based on restricted geometric transformations. *Inf. Sci.* **186**(1), 126–149 (2012)
24. Yan, F., Iliyasu, A.M., Sun, B., et al.: A duple watermarking strategy for multi-channel quantum images. *Quantum Inf. Process.* **14**(5), 1675–1692 (2015)
25. Yan, F., Iliyasu, A.M., Guo, Y.M., Yang, H.M.: Flexible representation and manipulation of audio signals on quantum computers. *Theor. Comput. Sci.* **752**, 71–85 (2018)
26. Abdullah, M., Iliyasu, P.C., Le, Q., Dong, F.Y., et al.: A framework for representing and producing movies on quantum computers. *Int. J. Quantum Inf.* **9**(6), 1459–1497 (2011)
27. Simona, C., Vasile, I.M.: Image segmentation on a quantum computer. *Quantum Inf. Process.* **14**(5), 1693–1715 (2015)

28. Jiang, N., Dang, Y., Wang, J.: Quantum image matching. *Quantum Inf. Process.* **15**(9), 3543–3572 (2016)
29. Zhang, Y., Lu, K., Gao, Y.: Q Sobel: a novel quantum image edge extraction algorithm. *Sci. China Inf. Sci.* **58**(1), 1–13 (2014). <https://doi.org/10.1007/s11432-014-5158-9>
30. Zhou, R.G., Liu, D.Q.: Quantum image edge extraction based on improved Sobel operator. *Int. J. Theor. Phys.* **58**(9), 2969–2985 (2019)
31. Fan, P., Zhou, R.G., Hu, W., Jing, N.: Quantum image edge extraction based on classical Sobel operator for NEQR. *Quantum Inf. Process.* **18**(1), 24 (2019)
32. Fan, P., Zhou, R.G., Hu, W.W., Jing, N.: Quantum image edge extraction based on Laplacian operator and zero-cross method. *Quantum Inf. Process.* **18**(1), 27 (2019)
33. Chetia, R., Boruah, S.M.B., Roy, S., Sahu, P.P.: Quantum image edge detection based on four directional sobel operator. In: International Conference on Pattern Recognition and Machine Intelligence (PREMI 2019). Lecture Notes in Computer Science, vol 11941. Springer, Cham, pp 532–540(2019)
34. Zhou, R.G., Yu, H., Cheng, Y., Li, F.X.: Quantum image edge extraction based on improved Prewitt operator. *Quantum Inf. Process.* **18**(9), 261 (2019)
35. Li, P., Shi, T., Lu, A., et al.: Quantum implementation of classical Marr–Hildreth edge detection. *Quantum Inf. Process.* **19**, 64 (2020). <https://doi.org/10.1007/s11128-019-2559-0>
36. Rosenfeld, A.: Digital Picture Processing. Academic Press, New York (1976)
37. Robinson, G.S.: Edge detection by compass gradient masks. *Comput. Graph. Image Process.* **6**, 492–501 (1977)
38. Khosropour, A., Aghababa, H., Forouzandeh, B.: Quantum division circuit based on restoring division algorithm. In: 2011 Eighth International Conference on Information Technology: New Generations. IEEE, pp. 1037–1040 (2011)
39. Wang, J., Jiang, N., Wang, L.: Quantum image translation. *Quantum Inf. Process.* **14**, 1589–1604 (2015)
40. Cuccaro, S.A., Draper, T.G., Kutin, S.A., Moulton, D.P.: A new quantum ripple-carry addition circuit. *arXiv:quant-ph/0410184* (2004)
41. Thapliyal, H., Ranganathan, N.: Design of efficient reversible binary subtractors based on a new reversible gate. In: 2009 IEEE Computer Society Annual Symposium on VLSI, IEEE, pp. 229–234 (2009)
42. Thapliyal, H., Ranganathan, N.: A new design of the reversible subtractor circuit. In: 2011 11th IEEE International Conference on Nanotechnology, IEEE, pp. 1430–1435 (2011)
43. Wang, D., Liu, Z.H., Zhu, W.N., Li, S.Z.: Design of quantum comparator based on extended general Toffoli gates with multiple targets. *Comput. Sci.* **39**(9), 302–306 (2012)
44. Tsai, H.M., Chang, L.W.: Secure reversible visible image watermarking with authentication. *J. Signal Process. Image Commun.* **25**, 10–17 (2010)
45. Yaghmaee, F., Jamzad, M.: Estimating watermarking capacity in Gray scale images based on image complexity. *EURASIP J. Adv. Signal Process.* (2010). <https://doi.org/10.1155/2010/851920>
46. Zhang, F., Zhang, X., Zhang, H.: Digital image watermarking capacity and detection error rate. *Pattern Recogn. Lett.* **28**, 1–10 (2008)
47. Gunjal, B.L., Manthalkar, R.R.: An overview of transform domain robust digital image watermarking algorithm. *J. Emerg. Trends Comput. Inf. Sci.* **2**(1), 37–42 (2010)
48. Liu, Q., Sung, A.H.: Image complexity and feature mining for stag analysis of least significant bit steganography. *Inf. Sci.* **178**, 21–36 (2008)
49. http://www.imageprocessingplace.com/root_files_V3/image_databases.htm

Publisher's Note Springer Nature remains neutral with regard to jurisdictional claims in published maps and institutional affiliations.